Nuclear Science and Techniques (2023) 34:164
https://doi.org/10.1007/s41365-023-01315-y

THUDose$_{PD}$: a three-dimensional Monte Carlo platform for phantom dose assessment

Xi-Yu Luo[1,2] · Rui Qiu[1,2] · Zhen Wu[1,3] · Shu-Chang Yan[1,2] · Zi-Yi Hu[1,2] · Hui Zhang[1,2] · Jun-Li Li[1,2]

Received: 3 April 2023 / Revised: 3 July 2023 / Accepted: 9 July 2023 / Published online: 14 November 2023

Abstract

Monte Carlo simulations are frequently utilized in radiation dose assessments. However, many researchers find the prevailing computing platforms to be intricate. This highlights a pressing need for a specialized framework for phantom dose evaluation. To address this gap, we developed a user-friendly radiation dose assessment platform using the Monte Carlo toolkit, Geant4. The Tsinghua University Phantom Dose (THUDose$_{PD}$) augments the flexibility of Monte Carlo simulations in dosimetric research. Originating from THUDose, a code with generic, functional, and application layers, THUDose$_{PD}$ focuses predominantly on anatomical phantom dose assessment. Additionally, it enables medical exposure simulation, intricate geometry creation, and supports both three-dimensional radiation dose analysis and phantom format transformations. The system operates on a multi-threaded parallel CPU architecture, with some modules enhanced for GPU parallel computing. Benchmark tests on the ICRP reference male illustrated the capabilities of THUDose$_{PD}$ in phantom dose assessment, covering the effective dose, three-dimensional dose distribution, and three-dimensional organ dose. We also conducted a voxelization conversion on the polygon mesh phantom, demonstrating the method's efficiency and consistency. Extended applications based on THUDose$_{PD}$ further underline its broad adaptability. This intuitive, three-dimensional platform stands out as a valuable tool for phantom radiation dosimetry research.

Keywords Monte Carlo · Phantom · Dose assessment · Voxelization · Three dimensional

1 Introduction

With the growing adoption of nuclear techniques in radiation protection and medical physics [1–6], accurate dose calculations for human phantoms have become indispensable. Phantom dose evaluations are pivotal in clinical practices such as radiotherapy, CT irradiation, X-ray radiography, and in radiation protection undertakings such as retrospective dose reconstruction and epidemiological studies [7–9]. Among the myriad techniques available, the Monte Carlo algorithm is esteemed as the gold standard for dose computation. This method encapsulates all physical processes and offers insights into transport processes by emulating particle-matter interactions [10]. Furthermore, the Monte Carlo approach facilitates the translation of microscopic mechanisms into macroscopic doses and exhibits higher precision over analytical algorithms, especially in heterogeneous geometries.

Many specialized Monte Carlo software tools are dedicated to phantom dose calculations, including GATE [11, 12], TOPAS [13, 14], and ARCHER [15–17]. Each

This work was supported by the National Natural Science Foundation of China (General Program) (Nos. 12175114, U2167209), the Foundation of Key Laboratory of Metrology and Calibration Technology (No. JLKG2022001C001), the Platform Development foundation of China Institute for Radiation Protection (No. YP21030101), the National Key R &D Program of China (No. 2021YFF0603600), and the Tsinghua University Initiative Scientific Research Program (No. 20211080081).

✉ Zhen Wu
wuzhen97@tsinghua.org.cn

[1] Department of Engineering Physics, Tsinghua University, Beijing 100084, China

[2] Key Laboratory of Particle and Radiation Imaging, Tsinghua University, Ministry of Education, Beijing 100084, China

[3] Nuctech Company Limited, Beijing 100084, China

has been meticulously researched and optimized for specific application domains. Other notable methods in this arena are MCNPX [18], FLUKA [19], and Geant4 [20]. While MCNPX and FLUKA largely operate via input card simulations, presenting a considerable workload for intricate geometries and source modeling, Geant4 stands out. Geant4 can accommodate more complex geometries and offers an extensive suite of functionalities, enhancing code flexibility. Written in C++, this open-source platform facilitates easier packaging and further development.

Geant4's flexibility leads to complexity. Writing and debugging code for a novel simulation requires considerable effort, and it can be difficult for researchers without significant programming experience. Additionally, although Geant4 supports phantom dose calculations, the user should import the geometry, dose algorithm, and tally score. If Geant4 can be packaged, then a specific function can be connected to the interface parameters, and a convenient and stable phantom dose calculation platform can be generated for specific phantom dose calculations.

Therefore, we developed a dedicated phantom dose calculation platform, THUDose$_{PD}$, based on the Geant4 toolkit, which includes the following:

- Preserve the underlying Geant4 code
- Visual user interface
- Provide various usage of phantom dose calculations
- Support CPU and GPU multi-threaded parallel computing
- Support three-dimensional visualization of geometry and results

The platform THUDose$_{PD}$ is tailored for pragmatic applications in clinical medicine and radiation protection. It boasts a user-friendly interface that facilitates complex geometric modeling and supports the transport of electrons, photons, neutrons, protons, and heavy ions. Additionally, the platform accommodates both single and dual phantom dose calculations, catering to the routine needs of medical physics and radiation protection. It offers methodologies for evaluating organ doses from both external and internal exposures. Keeping in sync with the evolution of phantoms, THUDose$_{PD}$ has implemented a procedure for the voxelization of polygon-mesh phantoms. The platform further enhances user experience by supporting three-dimensional visualization, spanning from the initial modeling phase to the final output. Grounded in a robust software architecture, THUDose$_{PD}$ has proven its merit in multiple research endeavors, covering scenarios of utmost interest to the majority of users and consistently offering convenience and stability.

2 Material and methods

The THUDose$_{PD}$ platform is based on THUDose [21], and was then expanded and developed for phantom dose calculation and three-dimensional visualization. The extended program has additional features, such as creating and converting phantoms, predefining standard source types, external and internal irradiation dose algorithms, and geometry visualization.

2.1 Universal MC program THUDose

THUDose is an in-house general Monte Carlo procedure written in C++ that wraps and extends the Geant4 toolkit. The platform operates via a Graphical User Interface (GUI) through which projects are built. In the background, XML files were saved using the settings set by the interface. The general, function, and application layers are the three layers that constitute THUDose. Figure 1 illustrates the system's overall structure. The four steps comprise a simulation in THUDose: geometric data, source definition, tally scores, and run parameters. The accompanying Fig. 2 shows the organizational structure of the interactive interface and a schematic.

In THUDose, the developers integrated physics lists derived from the cross-sectional libraries of both Geant4 and ENDF, selecting hadron and electromagnetic physics models for registration. This program was used to assess the transport of electrons, photons, protons, and neutrons. For material construction optimization, the platform provides two distinct strategies: The first approach utilizes the "Periodic Table" interface, allowing users to define materials on an individual basis. As an alternative, users can employ an Excel spreadsheet to craft a bill of materials, which facilitates the addition of materials in batches.

The source definition in THUDose is versatile, accommodating any particle type, energy, orientation, or spatial distribution. It allows the creation of multiple tallies for a single project, with each tally functioning independently. The software diligently logs energy deposition, flux, and particle count in the medium, segmented by particle type. To boost computational efficiency, the developers integrated parallel computing modules based on MPI. At present, THUDose can utilize up to 2000 parallel computing cores, contingent upon the computer's memory capacity. Furthermore, the software is equipped with GPU parallel computing functionalities for electrons and photons [8, 22]. The team plans to introduce support for GPU-based proton transport in the near future.

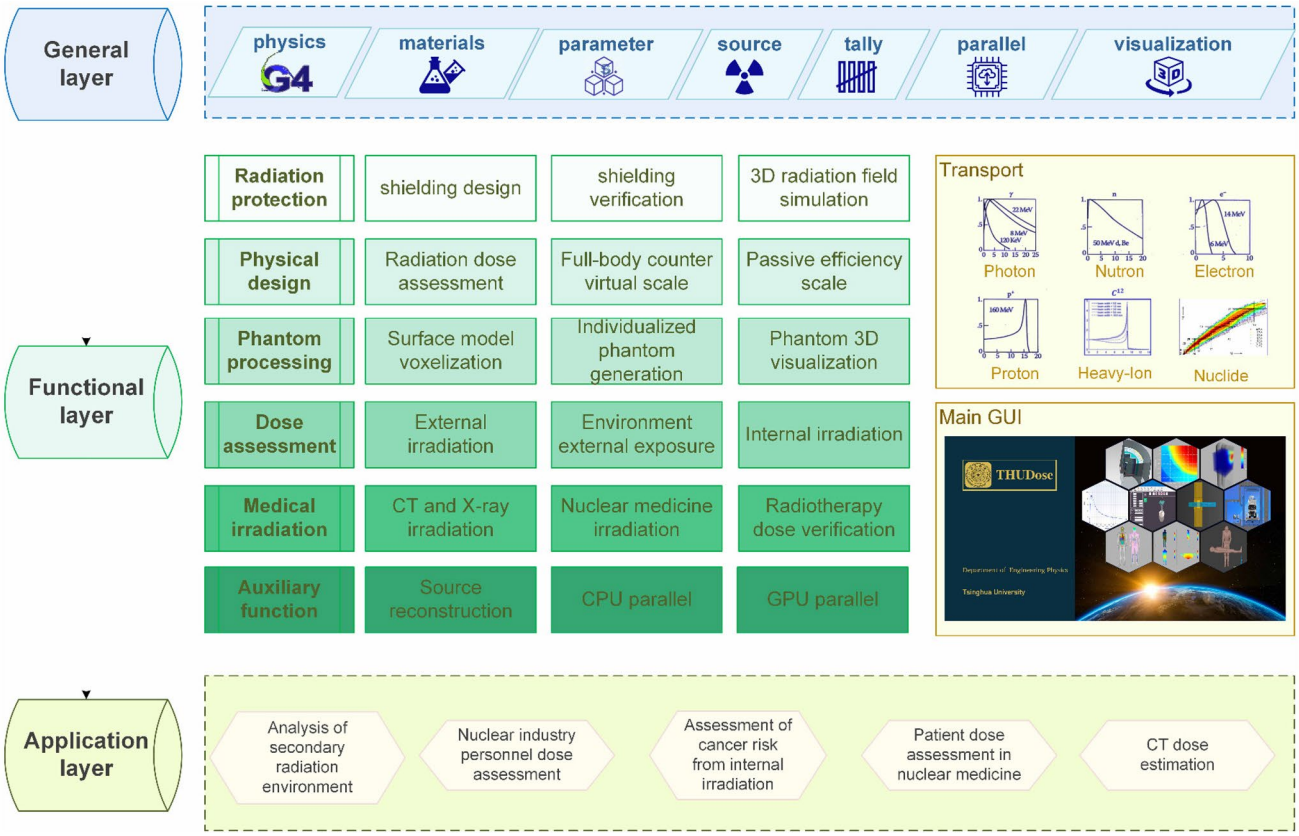

Fig. 1 (Color online) The overall structure of THUDose platform

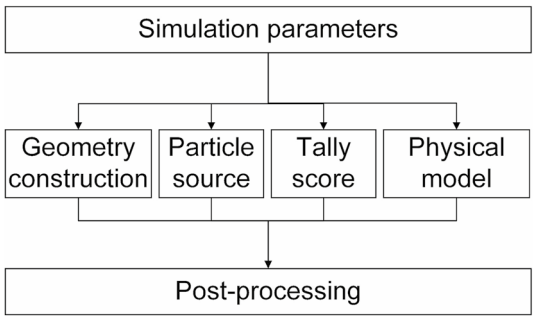

Fig. 2 The interactive interface organization structure of THUDose

2.2 Extensions for phantom dose assessment

Four processes comprise the majority of MC-based phantom dose assessments: phantom construction, particle transportation, dose calculation algorithm, and visualization. We investigated these four areas and developed a three-dimensional phantom dose assessment platform, THUDose$_{PD}$ based on THUDose.

2.2.1 Phantom construction and conversion

Currently, the voxel phantom stands as the predominant human anatomy model employed in radiation dose assessment. For precise dose assessment in intricate workplaces, it is vital to produce phantoms that offer adjustable sizes and postures. Such malleable models can be crafted using the Boundary Representation (BREP) geometric definition methods, which can take the form of non-uniform rational B-splines (NURBS), polygon meshes, or a combination thereof. Relative to voxel models, the BREP model offers a broader range of deformation operations. It can represent new anatomical structures for staff or patients even in the absence of comprehensive whole-body image data [23]. For the purpose of this work, all BREP models, which are expressed as polygon-mesh phantoms before final computations, are termed 'polygon-mesh phantom'.

Direct calculations on polygon mesh phantoms are unfeasible. Typically, they are converted into either voxels or tetrahedrons to facilitate particle transport [24, 25]. As of now, THUDose$_{PD}$ supports two such conversion techniques. However, given that tetrahedralization is not the focal point of this study, only the voxelization process is elucidated.

For the voxel phantom, THUDose$_{PD}$ can import data in a binary file format. Pertinent files include both a configuration file and binary file. Details, such as phantom's size, voxel's resolution, and phantom's central coordinates, are specified in the configuration file. Each voxel's value corresponds to a material index within a predefined list, indicating its material classification.

For polygon-mesh phantoms, THUDose$_{PD}$ offers a transformation procedure, termed voxelization. This method converts a three-dimensional object's geometric representation into a voxel format that closely mirrors the original. The resulting data captures both the surface and the inner geometric details. For rapid voxelization, THUDose$_{PD}$ employs OpenGL and utilizes the fragment shader in the rendering process to transition the intersection of triangles and voxels into sampling points. In parallel, computing techniques expedite the voxelization outcomes.

To enhance clinical efficacy, precise radiation dose evaluations based on actual patient CT scans are paramount. To this end, a phantom construction module was developed to load DICOM files, extract HU values, and subsequently transform them into densities and materials for ensuing calculations.

2.2.2 Particle transportation and source definition

The THUDose$_{PD}$ physical process is based on the THUDose physical model, facilitating the simulation and transport of photons, electrons, neutrons, protons, and heavy ions. The program has predefined the eight irradiation types highlighted in ICRU Publication 95: antero-posterior (AP), posterior-anterior (PA), left lateral (LLAT), right lateral (RLAT), rotational (ROT), isotropic (ISO), superior hemisphere semi-isotropic (SS-ISO), and inferior hemisphere semi-isotropic (IS-ISO). For X-ray radiography, which is prevalent in medical applications, the source has been parameterized. Users simply define the source axis distance, deflection angle, and field size to initiate vertebral tract sampling. In the context of CT, a butterfly filter specific to CT machines was developed to introduce a CT source [26]. Additionally, the program supports phase-space files for radiation field simulations and user-defined source parameters. Beyond these external exposure scenarios, the software offers two methodologies for internal exposure dose assessment: a swift computation approach based on specific absorbed fraction (SAF) values determined via the Monte Carlo algorithm and a more detailed method reliant on the nuclide spectrum.

2.2.3 Dose calculation algorithms

The software offers three calculation modes: external, internal, and environmental external radiation dose assessments [27]. Each mode facilitates computations of organ dose, effective dose, and three-dimensional dose distribution. Organ doses can be directly calculated by utilizing voxels for Monte Carlo transport. Furthermore, to support three-dimensional radiation dose evaluations, THUDose$_{PD}$ offers both voxel tally and mesh tally modes. In the voxel tally mode, when the input geometry is presented in voxels, the software generates a three-dimensional matrix identical in size to the geometry. It records physical quantities in each voxel grid and saves them in the respective element of the output matrix. This output matrix represents the three-dimensional statistical outcomes of the required physical quantities. Additionally, when there is a discrepancy between geometric and tally resolutions, data can be documented in the mesh tally mode, which derives from the G4MeshKernelRect class.

The calculations for organ and effective doses occur in the dose assessment module, termed as dose postprocessing. The aim here is to ascertain radiation-sensitive organ doses and then compute the effective dose, taking into account the tissue weight factor. Moreover, the software includes dose conversion coefficient computing capabilities, offering a theoretical foundation for radiation protection dose evaluations.

Assessing the dose for the red bone marrow is both vital and challenging in external radiation dose evaluations. THUDose$_{PD}$ adopts distinct methodologies for dose computations for typical organs and the red bone marrow. For organs excluding the red bone marrow, an average dose methodology is employed, as detailed in Eqs. (1–2):

$$D = \frac{\mathrm{d}\bar{\epsilon}}{\mathrm{d}m}, \tag{1}$$

$$D_{\mathrm{T}} = \frac{1}{m_{\mathrm{T}}} \int_{m_{\mathrm{T}}} D\mathrm{d}m, \tag{2}$$

where $\mathrm{d}\bar{\epsilon}$ denotes the mean energy imparted by ionizing radiation to matter of mass $\mathrm{d}m$, D denotes the absorbed dose, and m_{T} denotes the mass of an organ or tissue. These two equations were used to calculate the average absorbed dose of organ T, D_{T}. Furthermore, THUDose$_{PD}$ was used to directly count the energy deposition to obtain the absorbed dose of the organs with the exception of the red marrow and endosteum.

For the red bone marrow, THUDose$_{PD}$ provides three evaluation methods.

Direct method The approach considers the average dose of bones containing red marrow as the representative dose for the red marrow itself, termed as the bone-specific weighted average dose. This is computed as per the following formula, Eq. (3):

$$D_{RBM} = \frac{E_{RBM}}{m_{RBM}} = \frac{E_{Bone} \times r_{RBM}}{m_{RBM}} \tag{3}$$

The variable D_{RBM} represents the absorbed dose of the red bone marrow, while m_{RBM} signifies the mass of the red bone marrow. E_{RBM} and E_{bone} denote the energy deposits in the red bone marrow and bone, respectively. Lastly, r_{RBM} stands for the mass ratio of the red bone marrow to the bone.

3CFs-improved method Given that the equilibrium condition between the red bone marrow and trabecular bone is not met in phantoms, the *S* factor (or *KS* factor) is employed to calculate the dose of voxelized red bone marrow, termed the 3CFs method. Liu et al. [28] later refined this approach, resulting in the 3CFs-improved method. The absorbed dose D_{RMB} for the overall red bone marrow is the mass-weighted average of the red bone marrow dose at various locations. The associated formulas are presented in Eq. (4):

$$D^i_{RBM} = D^i_{SPA} \cdot \frac{\int \left(\frac{\mu_{en}}{\rho}(E)\right)_{RBM} \phi(E) KS(E) E \cdot dE}{\int \left(\frac{\mu_{en}}{\rho}(E)\right)_{SPA} \phi(E) E \cdot dE}, \tag{4}$$

where D^i_{RMB} and D^i_{SPA} denote the absorbed doses of the red bone marrow and spongiosa in bone *i*, the *KS* factor adopts the *KS* data of 44-year-old adults, *E* and $\phi(E)$ denote the photon energy and fluence in the spongiosa, respectively.

$$\overline{D}_{RBM} = \sum_i R^i \cdot D^i_{RBM} \tag{5}$$

The final average dose to the total red marrow is provided by Eq. (5), where R^i denotes the ratio of the mass of red marrow in bone i to the total mass of red marrow.

Dose-response function method We calculated the dose–response function method [29], as follows, in Eq. (6–7):

$$D(r_T, x) = \int_E \Phi(E, r_S, x) R(r_T \leftarrow r_S, x, E) dE, \tag{6}$$

$$D_{skel}(r_T) = \sum_x \frac{m(r_T, x)}{m(r_T)} D(r_T, x). \tag{7}$$

Bone-specific absorbed dose per particle fluence (Gy·cm^2) to red bone marrow and endosteum is a function of particle energy and skeletal region, i.e., $R(r_T \leftarrow r_S, x, E)$ in Eq. (6). The fluence of particles of energy *E* in the source tissue r_S of bone site *x*, $\Phi(E, r_S, x)$, was simulated by THUDose$_{PD}$. The absorbed dose to tissue r_T (red bone marrow) at bone site *x* was calculated using Eq. (6). Additionally, Eq. (7) is used to obtain the average absorbed dose of red marrow, where $m(r_T, x)$ and $m(r_T)$ denote the mass of tissue r_T at bone site *x* and the total mass of r_T, respectively.

For internal radiation dose computation, the software offers a quick estimation mode grounded on SAF values alongside a more detailed computation mode. The detailed approach utilizes Monte Carlo simulation, relying on the organ's nuclide spectrum. This strategy accommodates various models, working positions, and nuclide residence durations, employing the organ nuclide spectrum for the Monte Carlo simulation. Subsequently, the software calculates the equivalent and effective doses committed to the organs irradiated within the phantom. However, given this aspect beyond the main scope of this research, it will not be extensively discussed here.

2.2.4 Three-dimensional visualization

THUDose facilitates the visualization of geometry and particle trajectories in the 'wrl' format, compatible with most three-dimensional software. Moreover, THUDose$_{PD}$ enhances the three-dimensional visualization module, offering windows in four distinct views: perspective, front, side, and top. This advanced view supports the customization of visible slices and adjusts the displayed dose value ranges. For CAD geometries and polygon-mesh phantoms, THUDose$_{PD}$ allows imports in the 'ply' format and offers the ability to display components in a variety of colors. When it comes to voxel phantoms, THUDose$_{PD}$ features a display function for binary formats, where each organ can be distinctively showcased using a unique color set. In the realm of dose assessment, it is often pivotal to merge the geometry (or phantom) with the dose distribution, aiding in pinpointing high-dose locations and facilitating radiation risk analyses. THUDose$_{PD}$'s visualization module presents a solution that concurrently visualizes both geometry and dose distribution. The integration of isodose lines further aids users in their analyses. Furthermore, while organ doses are often rendered as non-intuitive tables or datasets, THUDose$_{PD}$ revolutionizes this by offering three-dimensional visualizations of organ doses, enabling the display of specific organs to streamline user comparisons and in-depth analyses.

2.3 Validation of THUDose$_{PD}$

The program's accuracy in phantom dose assessment underwent rigorous testing in several scenarios. THUDose$_{PD}$ was benchmarked against various ICRP publications, covering areas, such as external photon irradiation, external neutron irradiation, and internal electron irradiation, to authenticate

its physical processes and dose calculation methodologies. Additionally, by transforming the Chinese reference polygon-mesh phantom into voxels, discrepancies between the voxelized phantom and the established benchmark were scrutinized. Given the program's reliance on a three-dimensional visualization platform, its prowess in depicting the geometry and results in 3D is also showcased.

2.3.1 Benchmark against ICRP publications

The external irradiation benchmarking leveraged insights from ICRP publication 116. This evaluation contrasted dose conversion coefficients for ISO irradiation with monoenergetic photons and AP irradiation with monoenergetic neutrons. The internal irradiation benchmarking drew from the research of Zankl et al. [30, 31], which examined the SAF values of organs when subjected to electron and photon irradiation.

ICRP Publication 116 deduces reference conversion coefficients for both the effective dose and organ-absorbed doses under various external exposure conditions. This is based on the ICRP reference phantoms for both genders. It offers data from external beams of monoenergetic photons, electrons, positrons, and neutrons with configurations such as AP, PA, LLAT, RLAT, ROT, and ISO. In our assessment, the focus was on validating dose conversion coefficients specifically for the ICRP reference male, choosing monoenergetic photons and neutrons ranging from 10keV to 10GeV for the process.

Zankl et al. employed the ICRP reference male and the EGSnrc Monte Carlo program to deduce SAF values for photons and electrons, considering varied source organs and target organs. To ascertain the precision of SAF values derived using $\text{THUDose}_{\text{PD}}$, the ICRP reference male served as the basis for calculating the SAF values for electrons moving from the kidney to three distinct organs: the kidney itself, the adrenals, and the liver. The outcomes of this exercise were juxtaposed against Zankl's findings.

2.3.2 Polygon-mesh phantom voxelization

The polygon-mesh phantom was crafted by demarcating the organ boundaries of the voxel phantom using three-dimensional visualization software. This formed polygon mesh phantom boasts flexibility, allowing adjustments in height, weight, and posture. Once tailored, the modified polygon-mesh phantom was then imported into $\text{THUDose}_{\text{PD}}$ for dose calculations by transforming it back into a voxel phantom. Illustrating this with the Chinese polygon mesh reference male phantom (CRAM_{S}) as a case in point, the steps for voxelization can be seen in Fig. 3.

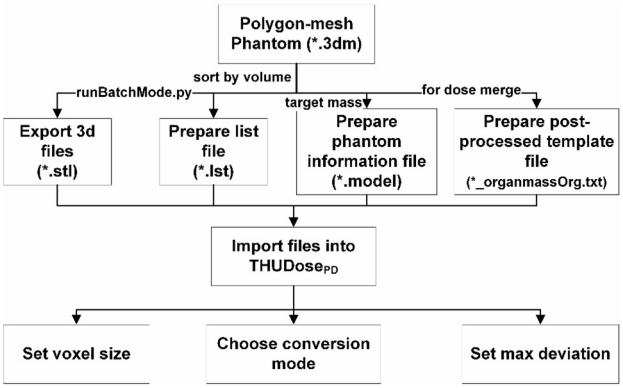

Fig. 3 Flowchart of the voxelization operation in $\text{THUDose}_{\text{PD}}$

First, the polygon-mesh phantom was adjusted using the three-dimensional modeling software Rhino to realize the target size and posture. Layers were added and named for each organ. The Python plug-in of Rhino was used to write scripts for batch export based on the polygon mesh phantom in $*$ *.3dm* form. Then, each organ was exported as an *stl* file with the same file name as the organ layer, and simultaneously the stl file list was exported, i.e., $*$ *.lst* text file, in which the file names are sorted from the largest to the smallest organ volume.

Subsequently, preparation of a phantom information file is necessary. This file should detail the index and anticipated weight of each organ. Moreover, during the post-processing phase of dose calculations - particularly when merging residual tissues—it is essential to identify the group to which an organ belongs. This type of information is then saved in a text file, denoted as ($*$ *organmassOrg.txt*).

The previously prepared files were then loaded into $\text{THUDose}_{\text{PD}}$. Users can set their preferred voxel size, expressed in millimeters (mm). Once the conversion mode is chosen, the program permits a maximum permissible deviation from the intended organ weight. It is worth noting that all organs are converted in descending order of size. Given this approach, conflicts may arise when smaller-volume organs intersect with larger ones. To address such conflicts, the program offers three resolution methods: overwriting, retaining, and randomizing

overwrite 'Overwrite' refers to the region where the conflict occurs is covered by the small volume organ that is converted later.

keep 'Keep' denotes that the current conversion result is maintained, and the small volume organ that will be converted later avoids the conflict area.

random 'Random' means that in conflict areas, small-volume organs are randomly covered.

The maximum deviation was used to ensure the upper limit of deviation between the voxelized organ mass and expected mass. The algorithm is realized by a loop that combines the corrosion and dilation algorithms. In this study, a polygon-mesh phantom CRAM$_S$ with a height of 170 cm and weight of 63 kg was voxelized. In the THUDose$_{PD}$ parameter configuration, the voxel resolution is 1.74 mm × 1.741 mm × 1.000 mm, the conversion mode is selected as 'overwrite,' and the maximum deviation is set to 2%. The results of the output voxel phantom, CRAM, were compared for organ mass and tested for the efficiency of the entire conversion process.

2.3.3 Three-dimensional dose assessment

A three-dimensional depiction of an indoor work environment was evaluated across several layers: the combined visualization of ray traces with geometry, integrated display of phantom files with three-dimensional dose distribution, and independent portrayal of phantom organ doses.

For the ray trace and geometry visualization test, a newborn phantom undergoing radiography was used. This phantom was subjected to a vertebral photon beam in an AP configuration. The distance between the source and the phantom's back was set at 100 cm, with a radiation field measuring 12.5 cm × 17.4 cm. To examine the integrated visualization of phantoms with three-dimensional dose distributions, and the distinct portrayal of organ doses, an external irradiation scenario was simulated using an isotropic point source. The chosen phantom for this test was a reference Chinese adult male. Positioned directly in front of the phantom was a ^{137}Cs point source, emitting energy at 661 keV. The three-dimensional dose distributions and organ doses were concurrently scored and then utilized in the visualization tests

3 Results

3.1 Benchmark against ICRP publication 116

In the study, THUDose$_{PD}$ was employed to determine the absorbed dose of the ICRP reference male subjected to ISO geometry. We focused our analysis on radiation-sensitive organs with significant radiation weight factors. The dose calculation for the phantom was executed using 100 CPU cores, transporting 1×10^8 particles in a parallel manner. Figure 4a displays the organ absorbed dose per fluence for 1×10^8 monoenergetic photons. Within this, both the 'Direct method' and '3CFs-improved method' were employed to assess the dose for the red bone marrow. These methods correspond to 'THUDose$_{PD}$' and 'THUDose$_{PD}$ − 3CF' in the legend, respectively. It is evident that our results align with the data from ICRP Publication 116. Notably, over 95% of our findings deviate from the ICRP Publication 116 data by less than 5%. The remaining deviations, particularly in results with larger discrepancies, are predominantly attributed to substantial statistical errors in both datasets at lower energies. We further juxtaposed the results of red bone marrow dose calculations using the 3CFs-improved method. This approach effectively rectified the elevated values observed in direct calculation methods in lower-energy areas, as confirmed by a prior study [28].

Using analogous calculation parameters as applied for photons, we determined the dose for neutrons irradiated with an AP geometry. Our focus was primarily on lung, skin, and brain tissues. Figure 4b presents the absorbed dose per fluence for 1×10^8 monoenergetic neutrons. When juxtaposed with ICRP data, our findings exhibited consistency across a broad spectrum of energy levels, ranging from keV to GeV.

ICRP Publication 133 offers data pertinent to internal exposure, including SAF values deduced via the Monte Carlo method. This represents the proportion of radiant energy originating from the source region that is absorbed per mass in the target region. Given that these ICRP data stem from Zankl's work, we reference them as 'Zankl et al.' in our subsequent analyses. Figure 5a and b illustrates the SAFs of electrons and photons traveling from the kidney to various target organs, including the kidney itself, the adrenal glands, and the liver. When the kidney functioned as both the source and target, the relative deviation in SAF values was capped at 3%. However, for target organs, such as the adrenal gland or liver, substantial deviations were observed at lower energies due to considerable statistical errors. Yet, the results closely matched at higher energy levels.

3.2 Polygon-mesh phantom voxelization

Upon voxelization of CRAM$_S$, we obtained the voxel phantom CRAM with dimensions of [276, 156, 1700] and a cumulative count of 73195200 voxels. This encapsulates 103 organs and tissues of the Chinese reference male. A comparison of voxelization results with the ground truth values is depicted in Fig. 6. The orange bars illustrate the genuine value, which signifies the anticipated mass of the organ prior to voxelization. Conversely, the green bars indicate the post-conversion mass of the respective voxel, following the transformation from polygon-mesh organs. The relative deviation between these two, as showcased in Fig. 6, aligns with the predetermined permissible deviation threshold of 2%.

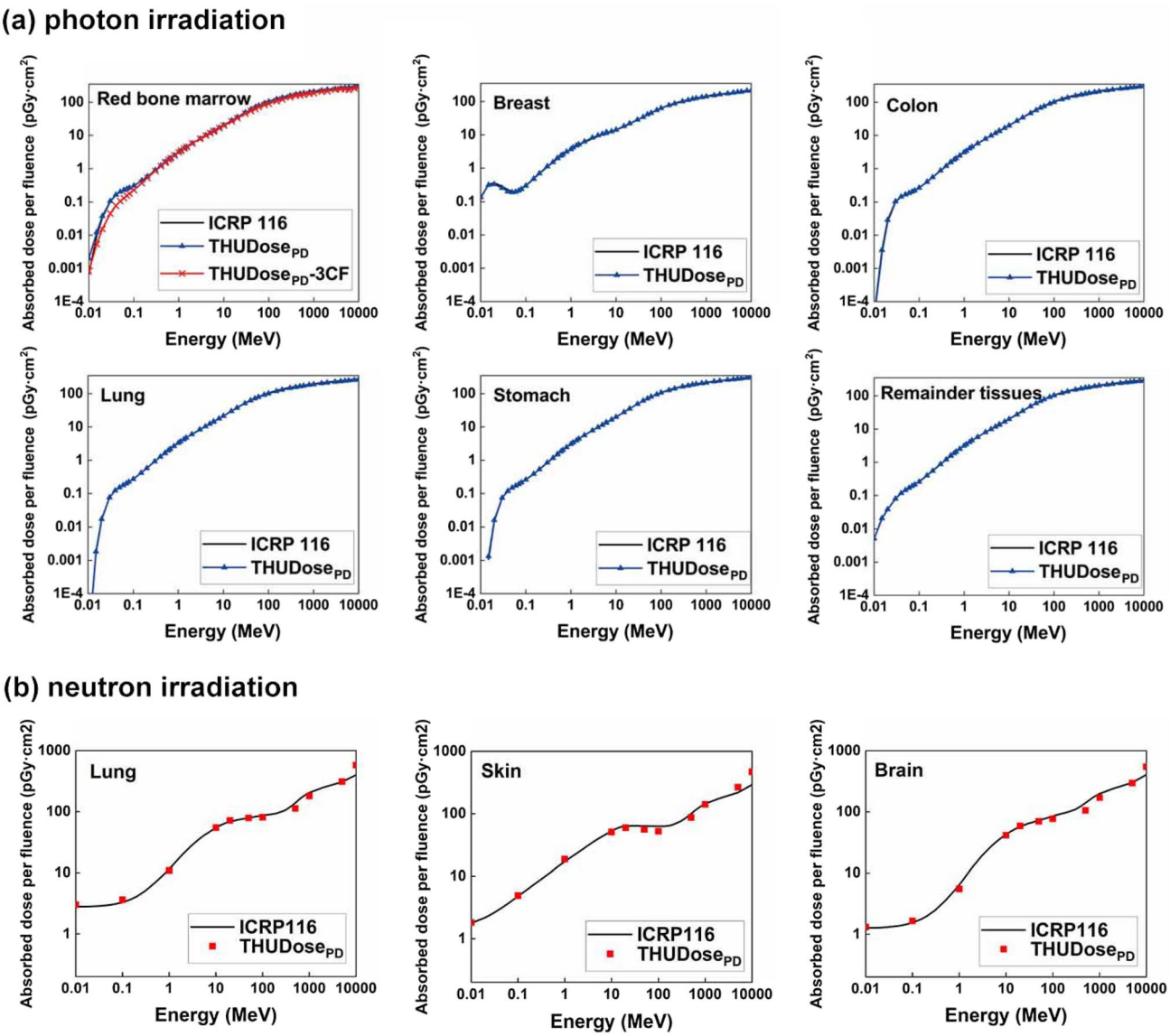

Fig. 4 (Color online) (**a**) Organ absorbed dose per fluence for mono-energetic photons incident in ISO. (**b**) Organ absorbed dose per fluence for mono-energetic neutron incident in AP

Furthermore, we chose four phantoms from the Chinese adult standing phantom repository for the voxelization process. Their respective conversion durations are detailed in Table 1. The process to voxelize an adult phantom, containing between 50 to 90 million voxels, spans approximately 2–3 minutes, contingent on the phantom's size.

The resultant visualization file is outputted in the $*$ *.wrl* format, allowing users to leverage any three-dimensional visualization software for analysis. This includes evaluating object coordinates, radiation field dimensions, and other pertinent data. The geometry and ray trajectories of neonatal phantom radiographs focusing on the pelvis are presented in Fig. 7a. Within THUDose$_{PD}$, the 'run parameter' dictates whether the geometry is generated. If geometry generation is approved, then the default history of transported particles is set to ensure that the simulation scene can be rendered with minimal computational effort. The amalgamation and display of tracks and geometries significantly streamline project examinations.

Dose distribution within a phantom offers the most straightforward approach to three-dimensional dose evaluation. The amalgamation of the phantom and its three-dimensional dose representation facilitates this methodology. Figure 7b–c illustrates the three-dimensional dose distribution from a ^{137}Cs point source utilizing an AP geometry. Figure 7b presents four distinct display modes of the phantom and dose: (i) showcases the phantom's cross-sectional view, (ii) emphasizes the dose distribution, (iii) integrates both

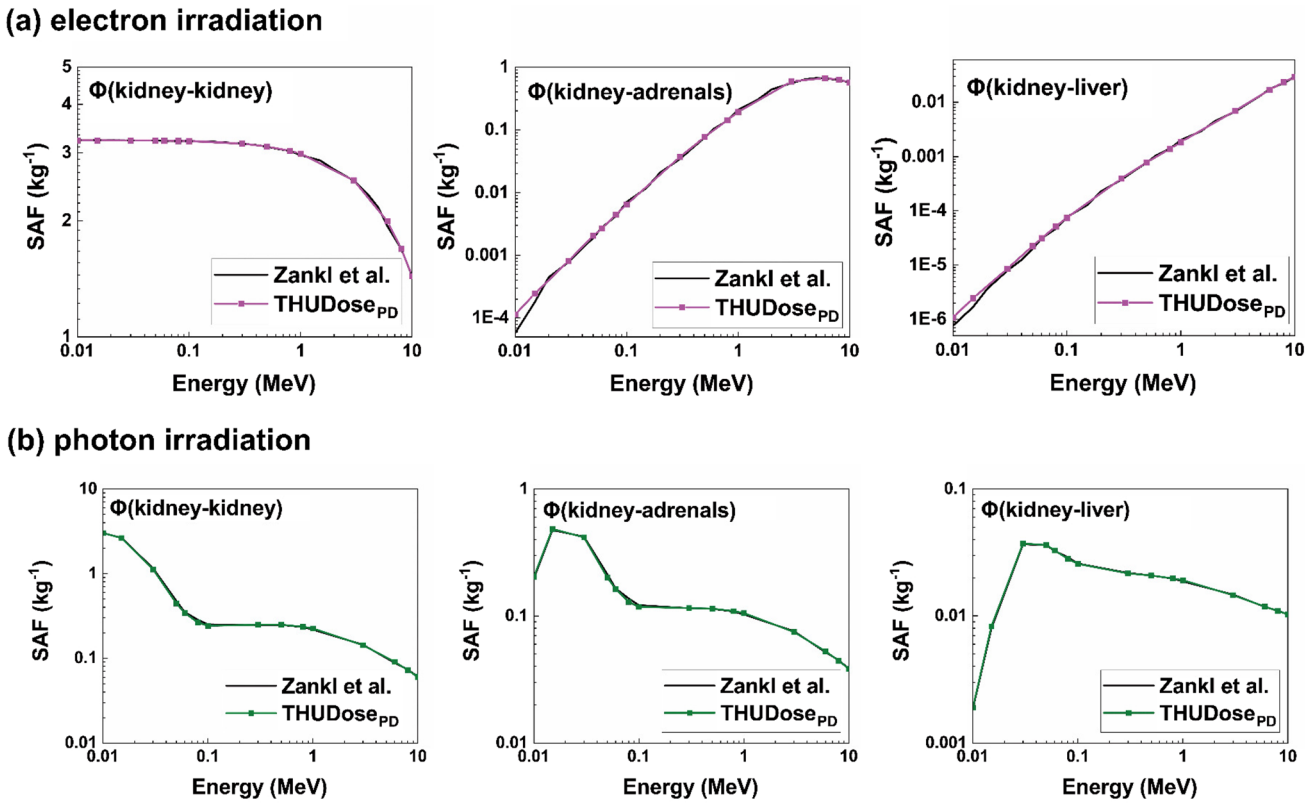

Fig. 5 (Color online) (**a**) SAF values of electrons with kidney as the source organ, (**b**) SAF values of photons with kidney as the source organ

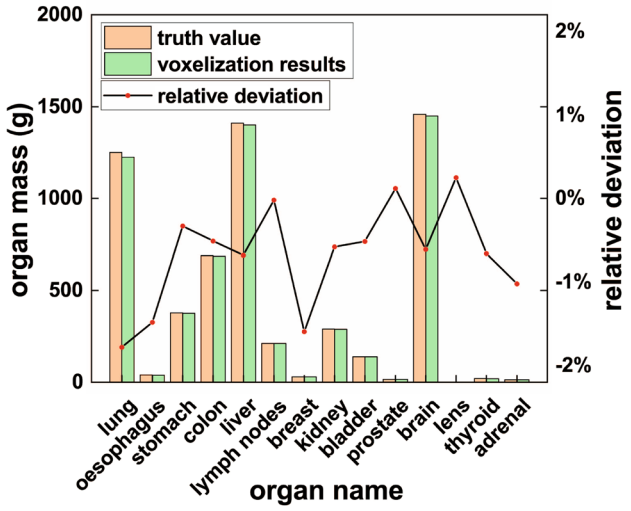

Fig. 6 (Color online) Comparison of organ mass between voxelization results and truth values

phantom and dose visuals, and (iv) supplements (iii) with isodose lines. This versatile visualization technique assists users in analyzing radiation field metrics and dose layouts. A comprehensive three-dimensional perspective, encompassing perspective, front, lateral, and top views complemented by a color scale, is portrayed in Fig. 7c.

Additionally, THUDose$_{PD}$ introduces a feature for visualizing the three-dimensional organ dose distribution. Figure 7d displays the organ doses across various energy spectra. Each organ's dose is represented by a distinct color, signifying its specific dose amount.

Table 1 Voxelization cost time

Phantom	Phantom size	Conversion time (s)
H155M45	[258 146 1552]	120
H165M67	[282 168 1650]	150
H175M75	[288 184 1752]	156
H185M84	[294 176 1850]	196

4 Conclusion

In this research, we introduced the Monte Carlo simulation platform, THUDose$_{PD}$, tailored for three-dimensional phantom dose evaluations. This platform is adept at parallel

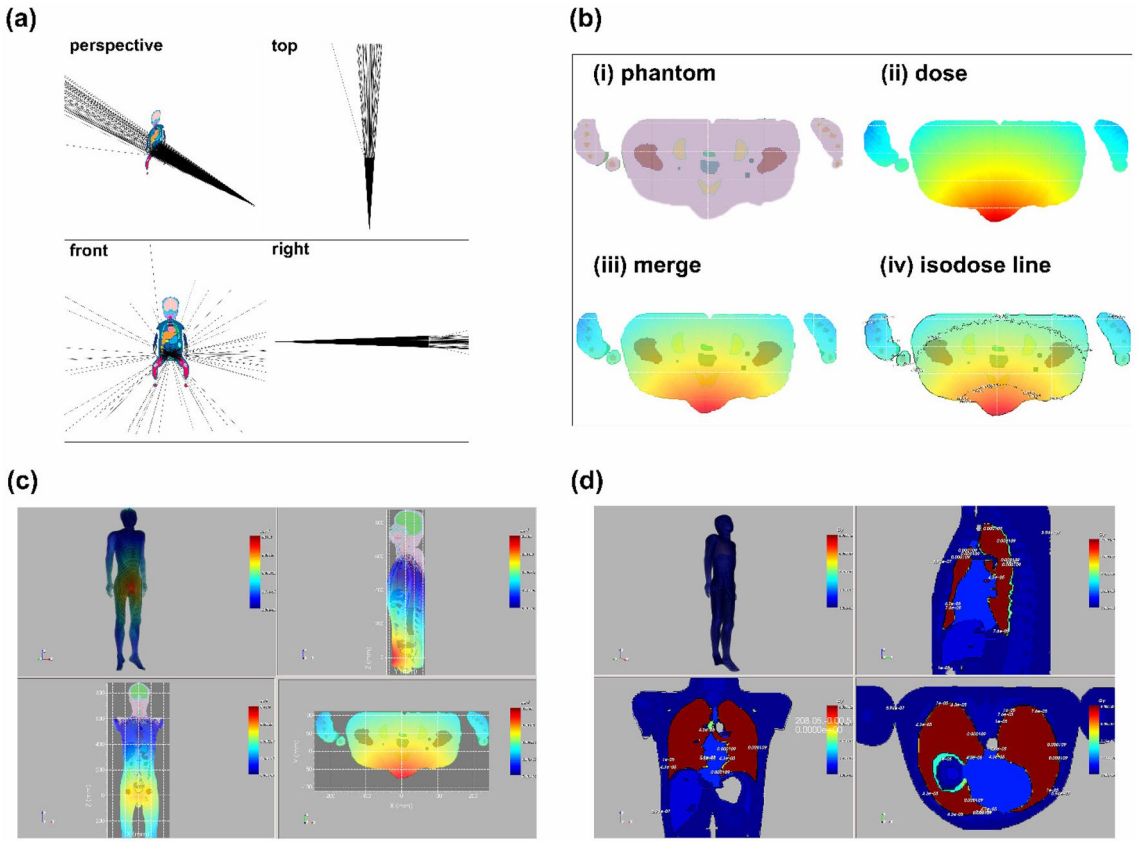

Fig. 7 (Color online) (**a**) Geometry and track of neonatal pelvic X-ray photography, (**b**) fused display of voxel phantom and three-dimensional dose distribution, (**c**) Three-dimensional dose distribution of isotropic point source irradiation with ^{137}Cs, and (**d**) three-dimensional organ dose of a random energy spectrum

processing of photons, electrons, neutrons, and other particle types using both CPU and GPU. It offers a plethora of methods for defining sources and geometries. Significantly, it incorporates a voxelization technique for the polygon mesh phantom, achieving phantom conversions with a precision under 2% in approximately 2 minutes. Moreover, it supports calculations for both external and internal organ irradiation doses and enables visualization of three-dimensional geometry, particle trajectories, and dose distributions. Catering to an array of requirements in three-dimensional phantom dose assessments, this platform proves invaluable for both radiation protection and clinical scenarios. Currently, its applications span personal dose evaluations [32], environmental exposure dose coefficients [27], internal radiation cancer risk studies, dosimetric reconstructions for a radiological mishap in Nanjing, China [33], CT radiation dose evaluations [26, 34], and more, underlining its substantial potential in the field.

Author contributions All authors contributed to the study conception and design. Material preparation, data collection and analysis were performed by Xi-Yu Luo, Rui Qiu, Zhen Wu, Shu-Chang Yan, and Zi-Yi Hu. The first draft of the manuscript was written by Xi-Yu Luo and all authors commented on previous versions of the manuscript. All authors read and approved the final manuscript.

Data availability The data that support the findings of this study are openly available in Science Data Bank at https://doi.org/10.57760/sciencedb.10919 and https://cstr.cn/31253.11.sciencedb.10919.

Declarations

Conflict of interest The authors declare that they have no competing interests.

References

1. W.M. Sun, N. Du, W.D. Tian et al., Secondary and activated x (γ) radiation of sphic particle therapy facility. Nucl. Sci. Tech. **32**, 42 (2021). https://doi.org/10.1007/s41365-021-00870-6
2. C.Y. Li, X.B. Xia, J. Cai et al., Radiation dose distribution of liquid fueled thorium molten salt reactor. Nucl. Sci. Tech. **32**, 22 (2021). https://doi.org/10.1007/s41365-021-00857-3
3. C.M. Niu, M.H. Li, J.R. Dai, Cage-like radiotherapy system for noncoplanar radiotherapy. Nucl. Sci. Tech. **32**, 12 (2021). https://doi.org/10.1007/s41365-021-00848-4

4. Y. Wang, Y.Y. Liu, B. Wu et al., Experimental investigation on the radiation background inside body counters. Nucl. Sci. Tech. **33**, 20 (2022). https://doi.org/10.1007/s41365-022-01004-2
5. J.Y. Chen, D.Q. Wang, X.D. Zhang et al., Sparing lung tissue with virtual block method in vmat planning for locally advanced non-small cell lung cancer. Nucl. Sci. Tech. **33**, 51 (2022). https://doi.org/10.1007/s41365-022-01033-x
6. S.C. Huang, H. Zhang, K. Bai et al., Monte carlo study of the neutron ambient dose equivalent at the heavy ion medical machine in Wuwei. Nucl. Sci. Tech. **33**, 119 (2022). https://doi.org/10.1007/s41365-022-01093-z
7. Z. Peng, N. Gao, B. Wu et al., A review of computational phantoms for quality assurance in radiology and radiotherapy in the deep-learning era. J. Radiat. Prot. Res **47**, 111–133 (2022). https://doi.org/10.14407/jrpr.2021.00402
8. A.K. Hu, R. Qiu, H. Liu et al., Thubrachy: fast monte carlo dose calculation tool accelerated by heterogeneous hardware for high-dose-rate brachytherapy. Nucl. Sci. Techniq. (2021). https://doi.org/10.1007/s41365-021-00866-2
9. J.L. Chen, S.J. Yun, T.K. Dong et al., Studies of the radiation environment on the mars surface using the geant4 toolkit. Nucl. Sci. Tech. **33**, 11 (2022). https://doi.org/10.1007/s41365-022-00987-2
10. D. Rogers, Fifty years of monte carlo simulations for medical physics. Phys. Med. Biol. **51**, R287 (2006). https://doi.org/10.1088/0031-9155/51/13/R17
11. G. Santin, D. Strul, D. Lazaro et al., Gate: a geant4-based simulation platform for pet and spect integrating movement and time management. IEEE Trans. Nucl. Sci. **50**, 1516–1521 (2003). https://doi.org/10.1109/TNS.2003.817974
12. S. Jan, D. Benoit, E. Becheva et al., Gate v6: a major enhancement of the gate simulation platform enabling modelling of ct and radiotherapy. Phys. Med. Biol. **56**, 881–901 (2011). https://doi.org/10.1088/0031-9155/56/4/001
13. J. Perl, J. Shin, J. Schümann et al., TOPAS: an innovative proton Monte Carlo platform for research and clinical applications. Med. Phys. **39**(11), 6818–6837 (2012). https://doi.org/10.1118/1.4758060
14. B. Faddegon, J. Ramos-Mendez, J. Schuemann et al., The topas tool for particle simulation, a Monte Carlo simulation tool for physics, biology and clinical research. Physica Med. **72**, 114–121 (2020). https://doi.org/10.1016/j.ejmp.2020.03.019
15. X.G. Xu, T. Liu, L. Su et al., Archer, a new monte carlo software tool for emerging heterogeneous computing environments. Ann. Nucl. Energy **82**, 2–9 (2015). https://doi.org/10.1016/j.anucene.2014.08.062
16. L. Su, Y. Yang, B. Bednarz et al., Archerrt - a gpu-based and photon-electron coupled monte carlo dose computing engine for radiation therapy: software development and application to helical tomotherapy. Med. Phys. **41**, 071709 (2014). https://doi.org/10.1118/1.4884229
17. D.P. Adam, T. Liu, P.F. Caracappa et al., New capabilities of the monte carlo dose engine archer-rt: Clinical validation of the varian truebeam machine for vmat external beam radiotherapy. Med. Phys. **47**, 2537–2549 (2020). https://doi.org/10.1002/mp.14143
18. T. Goorley, M. James, T. Booth, et al., Initial mcnp6 release overview - mcnp6 version 1.0. Los Alamos, NM: Los Alamos National Laboratory. https://doi.org/10.2172/1086758
19. C. Ahdida, D. Bozzato, D. Calzolari et al., New capabilities of the fluka multi-purpose code. Front. Phys. **9**, 705 (2022). https://doi.org/10.3389/fphy.2021.788253
20. J. Allison, K. Amako, J. Apostolakis et al., Geant4 developments and applications. IEEE Trans. Nucl. Sci. **53**, 270–278 (2006). https://doi.org/10.1109/TNS.2006.869826
21. L. Xi-yu, Q. Rui, W. Zhen et al., Development and application of radiation protection calculation software thudose. Mod. Appl. Phys. **12**, 6 (2021). https://doi.org/10.12061/j.issn.2095-6223.2021.020203
22. Y.S.Q.R.Z.H.L.J. WU Zhen, LU Wei, Development of a gpu-accelerated photon-electron coupled transportation monte carlo code and its application. J.f Harbin Eng. Univ. **43**, 9 (2022).https://doi.org/10.11990/jheu.202206028
23. G. Gualdrini, P. Ferrari, Handbook of anatomical models for radiation dosimetry. Radiat. Prot. Dosimetry. **143**, 125–127 (2011). https://doi.org/10.1093/rpd/ncq333
24. W. Kainz, E. Neufeld, W.E. Bolch et al., Advances in computational human phantoms and their applications in biomedical engineering-a topical review. IEEE Trans. Radiat. Plasma Med. Sci. **3**, 1–23 (2019). https://doi.org/10.1109/TRPMS.2018.2883437
25. Y.S. Yeom, J.H. Jeong, M.C. Han et al., Tetrahedral-mesh-based computational human phantom for fast Monte Carlo dose calculations. Phys. Med. Biol. **59**, 3173–3185 (2014). https://doi.org/10.1088/0031-9155/59/12/3173
26. R.Y. Ma, R. Qiu, Z. Wu et al., Development of Chinese mesh-type pediatric reference phantom series and application in dose assessment of Chinese undergoing computed tomography scanning. Phys. Med. Biol. **66**, 195002 (2021). https://doi.org/10.1088/1361-6560/ac1ef1
27. W. Lu, R. Qiu, Z. Wu et al., Calculation of conversion coefficients using Chinese adult reference phantoms for air submersion and ground contamination. Phys. Med. Biol. **62**, 2276–2314 (2017). https://doi.org/10.1088/1361-6560/aa5c31
28. L. Liu, Z. Zeng, J. Li et al., An icrp-based chinese adult male voxel model and its absorbed dose for idealized photon exposures-the skeleton. Phys. Med. Biol. **54**, 6675 (2009). https://doi.org/10.1088/0031-9155/54/21/015
29. N. Petoussi-Henss, W.E. Bolch, K.F. Eckerman et al., Conversion coefficients for radiological protection quantities for external radiation exposures. Ann. ICRP **39**, 1–257 (2010). https://doi.org/10.1016/j.icrp.2011.10.001
30. M. Zankl, H. Schlattl, N. Petoussi-Henss et al., Electron specific absorbed fractions for the adult male and female icrp/icru reference computational phantoms. Phys. Med. Biol. **57**, 4501 (2012). https://doi.org/10.1088/0031-9155/57/14/4501
31. J.E. Valentin, Icrp publication 103: the 2007 recommendations of the international commission on radiological protection. Ann. ICRP **37**, 1–332 (2007). https://doi.org/10.1016/j.icrp.2007.10.003
32. X. Luo, R. Qiu, Z. Wu et al., A body-size-dependent series of chinese adult standing phantoms for radiation dosimetry. J. Radiol. Prot. **43**, 011501 (2023). https://doi.org/10.1088/1361-6498/acad0d
33. W. Lu, Z. Wu, R. Qiu et al., Physical dosimetric reconstruction of a radiological accident at nanjing (china) for clinical treatment using thudose. Health Phys. **113**, 327–334 (2017). https://doi.org/10.1097/HP.0000000000000711
34. R. Li, Q. Rui, W. Zhen et al., Simulation and analysis of ct examination doses to typical patients based on Chinese reference human phantoms. Chin. J. Radiol. Med. Protect. **38**, 7 (2018). https://doi.org/10.3760/cma.j.issn.0254-5098.2018.12.011